

Journal of Biomedical Optics

SPIEDigitalLibrary.org/jbo

Fast vascular component of cortical spreading depression revealed in rats by blood pulsation imaging

Victor Teplov
Artem Shatillo
Ervin Nippolainen
Olli Gröhn
Rashid Giniatullin
Alexei A. Kamshilin

Fast vascular component of cortical spreading depression revealed in rats by blood pulsation imaging

Victor Teplov,^a Artem Shatillo,^b Ervin Nippolainen,^a Olli Gröhn,^b Rashid Giniatullin,^{b,c} and Alexei A. Kamshilin^{a,*}

^aUniversity of Eastern Finland, Department of Applied Physics, P.O. Box 1627, Yliopistonranta 1 F, 70210 Kuopio, Finland

^bUniversity of Eastern Finland, Department of Neurobiology, A. I. Virtanen Institute, P.O. Box 1627, Neulaniementie 2, 70211 Kuopio, Finland

^cKazan Federal University, Lab of Neurobiology, Kazan 420000, Russia

Abstract. Cortical spreading depression (CSD) is a slowly propagating wave of depolarization of neurons and glia and has a less characterized vascular component. CSD is a commonly used phenomenon to test new methods of live brain imaging. Application of a blood pulsations imaging (BPI) technique to study of CSD induced with high-potassium solution in rat cortex allowed us to visualize for the first time the novel vascular component of a CSD wave. In our study, this wave component propagated in the limited part of the cortex along the bow-shaped trajectory in sharp contrast with concentric development of CSD measured by concurrently applied optical intrinsic signal (OIS) imaging technique. It was associated with a significant increase of the blood pulsations amplitude (BPA), started with a delay of 20 to 90 s comparing to signal measured with OIS, and propagated 40% faster than OIS signal. These findings suggest that the BPA and slower change of the cerebral blood volume are not directly related to each other even though both characterize the same vascular system. Our study indicates that the BPI technique could be used for characterization of the new pulsatile vascular component of CSDs in animal models of migraine, stroke, and brain trauma. © 2014 Society of Photo-Optical Instrumentation Engineers (SPIE) [DOI: [10.1117/1.JBO.19.4.046011](https://doi.org/10.1117/1.JBO.19.4.046011)]

Keywords: image processing; biomedical optical imaging; brain stimulation; cortical spreading depression.

Paper 130775RR received Oct. 28, 2013; revised manuscript received Mar. 21, 2014; accepted for publication Mar. 25, 2014; published online Apr. 11, 2014.

1 Introduction

In the past three decades, investigation of cortical spreading depression (CSD) attracted a lot of attention since it is considered to be involved in migraine with aura, epilepsy, and ischemic stroke.¹ CSD is a complex pathophysiological phenomenon involving transient suppression of neuronal activity, which can be characterized by an electroencephalogram depression.² It is also accompanied by deflection of direct current (DC) potential³ and changes of blood flow.^{4–6} Optical methods are among most powerful tools to detect the temporal and spatial changes of an experimentally evoked CSD. CSD has been experimentally elicited with a variety of chemical, electrical, and mechanical stimuli in various animals.⁷ A wide variety of methodologies including observation of pial vessels diameter,^{8–10} optical intrinsic signals (OIS) imaging,^{5,10–17} intravascular dye imaging,¹² laser speckle contrast (LSC) imaging,^{18–20} and laser Doppler flowmetry (LDF),^{9,10,19–21} have been used to study spatio-temporal characteristics of CSD. Injection of K⁺ into cerebral cortex is a common way to induce the phenomenon of CSD.^{5,9,13,17,19,21} Most researchers report that a CSD wave arises from the site of initiation after a latency ranging from tens of seconds to several minutes and then spreads uniformly (as centering rings) through the cortical tissue at a rate of 2 to 5 mm/min.^{5,11–14,19}

Both OIS and LSC imaging techniques enable visualization of CSD at the cortex with high spatial and temporal resolution.^{10–14,18,19} OIS system measures wavelength-dependent

changes in cortical light reflectance induced by changes in concentration of oxyhemoglobin and deoxyhemoglobin, which are related with cerebral blood volume (CBV).^{4,5} LSC system enables monitoring of light-reflectance changes related to movement of red blood cells, thus measuring the cerebral blood flow.^{18–20} Therefore, optical imaging systems provide measurements of the vascular component of the CSD phenomenon while detecting the DC shift by the local field potential (LFP) allows monitoring the changes of its neuronal component.

Spatially resolved two-dimensional (2-D) mapping of the oxygenated hemoglobin distribution over the skin of human subjects was demonstrated *in-vivo* using photoplethysmographic (PPG) imaging, which exploits modulation of the reflected light intensity at the heartbeat frequency when the subject is illuminated by light at two to three different wavelengths.^{22,23} PPG imaging technique with improved signal-to-noise ratio (SNR) (called blood pulsations imaging, BPI) was recently proposed by our group allowing mapping not only the amplitude of blood pulsations but also spatial distribution of the pulsations phase within a cardiac cycle.^{24,25} Even though the optics and electronics for BPI implementation is the same as for OIS imaging, the data processing in these systems is completely different. OIS imaging reveals slowly varying (in the time scale of few seconds) changes in the recorded frames of the reflected light, which are assumed to be proportional to changes in blood volume.^{4,5} In contrast, the BPI technique reveals the signals correlated in time with the cardiac activity

*Address all correspondence to: Alexei A. Kamshilin, E-mail: alexei.kamshilin@uef.fi

for each heartbeat.²⁵ Although the temporal modulation of the signal at the heartbeat frequency in OIS is considered as the noise (consequently, the removal of this modulation leads to the SNR improvement^{26,27}), in BPI such a modulation is used as a signal. Thus, the BPI technique brings new readouts of neurovascular activity as it measures the amplitude of blood volume pulsations, which is not necessarily related to the slow changes in blood volume observed by OIS imaging.

The aim of this study is to examine applicability of the BPI system to detection of artificially induced CSD in the cortex of rats and to compare the obtained results with OIS images and LFP recordings. We found that CSD waves are revealed by the BPI technique as significant increase of the amplitude of blood pulsations during the CSD event while the relative phase of pulsations is insignificantly changed. The revealed CSD wave propagates along a bow-shaped trajectory, which differs from that revealed by OIS. The speed of BPI-revealed wave is higher than that of OIS-revealed wave. Moreover, the delay between CSD registration by BPI and LFP recordings is different for the primary and secondary events in the case of excitation of multiple CSD waves. All these findings allow us to conclude that BPI measures a new vascular component of CSD phenomenon, which is different from the vascular component measured by commonly available imaging techniques, such as OIS, LSC, and LDF.

2 Method and Materials

2.1 Experimental Setup

The study of the CSD events in rats' cortex involved the preparation of the experimental setup and the animal for the measurements. The experimental setup for concurrent use of BPI, OIS imaging, and electrophysiological recordings comprises of two principal parts: recording systems (optical and electrophysiological) and the animal unit (stereotaxis, heating control, etc.) with rat. The schematic drawing of the whole experimental setup is shown in Fig. 1(a). The optical system for implementation of both the BPI and OIS techniques includes two optical elements: a photodetector and an illuminator. As the photodetector, we used a digital, monochrome 8-bit CMOS camera (EO-1312, Edmund Optics, Barrington, New Jersey) with attached camera lens (18 to 108 mm focal length,

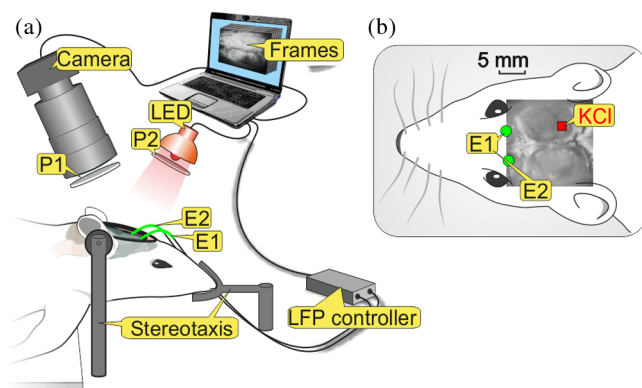


Fig. 1 (a) Layout of the experimental setup with blood pulsation imaging of the rat cortex: P1, P2—polarizers, E1, E2—local field potential (LFP) electrodes, implanted into the right and left hemispheres, LED—light emitted diode ($\lambda = 920$ nm). (b) Schematic view of the rat head with overlaid raw camera image showing the KCl-application site and the location of the LFP electrodes E1, E2.

Canon, Tokyo, Japan). Video frames with size of 300×300 pixels were recorded at the rate of 60 frames/s.

As illuminator, we used a conventional light-emitting diode (LED) (H2A1-H920, Røithner Lasertechnik GmbH, Wien, Austria) that generated the light at the wavelength of 920 nm. This wavelength was chosen because we found that the SNR for rat cortex illumination is higher compared with illumination by LEDs operating at the wavelength from the visible range. Moreover, the penetration depth in the tissue of the infrared light is larger than that of the visible light.²⁸ The optical power of the LED is 80 mW, the wavelength bandwidth is 60 nm. The illuminator provided uniform illumination of the open skull area sizing 3×3 cm² at a distance between the subject and video camera of about 8 cm. Note that during video recording the lens diaphragm and the camera exposure time were adjusted so that the recorded frames did not contain saturated pixels (the maximal pixel value is 255 for 8-bit camera), but were as bright as possible. During the experiment, the ambient illumination was much lower than that provided by the illuminator.

The camera was mounted in a vertical position for recording the focused image of the rat's cortex, and it was fixed so that the angle between the optical axis of the camera and illuminator was minimal. The generated light was linearly polarized by means of a polarizer P1 [Fig. 1(a)] attached to the illuminator. The polarizer P2 was attached to the camera lens so that its transmission axis was oriented orthogonal to the polarization vector of the illuminating light. By using crossed polarizations, we reject the light reflected from the cortex surface-air interface. The camera was connected to a personal computer (PC) through the universal serial bus (USB) port providing the frames transfer for downloading to the computer hard drive. The illuminator also was connected to the PC through other USB port for powering of the LEDs, which benefits in the full portability of the video recording system.

The electrophysiological recording was done by conventional LFPs technique using a BrainAmp MR Plus system (Brain Products GmbH, Munich, Germany). Signal from the electrodes E1 and E2 [Fig. 1(b)] was amplified, notch-filtered at 50 Hz and digitized with sampling rate of 5000 Hz. LFP recording system was connected to the same PC for real-time processing, monitoring, and storage of the data.

2.2 Animal Preparation

Male Wistar rats 12 to 14 weeks old ($n = 6$, National Laboratory Animal Center of the University of Eastern Finland) were used in this study. During surgical preparation procedures all rats were anesthetized with isoflurane (4% for induction and 2% for maintenance during surgery) in 70% N₂—30% O₂ mixture. Xylocaine gel was used to alleviate pain in incision and pressure points. Body temperature was maintained at approximately 37°C with a heating pad. Anesthetized rat was mounted into a stereotactic frame (David Kopf Instruments GmbH, Düsseldorf, Germany) for craniectomy and guided electrode implantation. The frame also served to avoid motion artifacts during the recording session after the surgery.

For optical imaging, the scalp was excised and skull bones were cleaned from soft tissues remainders with hydrogen peroxide solution (Sigma Aldrich GmbH, Munich, Germany). Parietal bones were bilaterally removed from sigma to bregma using a dental drill. The central strip of the skull along the suture was left untouched to avoid damaging of the sagittal sinus. Maximum care was taken to preserve integrity of meninges

and prevent bleeding. After the surgery, isoflurane anesthesia was switched to urethane (1.25 g/kg, Sigma Aldrich GmbH, Germany).

For LFP recordings two insulated tungsten 50- μm diameter electrodes (California Fine Wire, Grover Beach, California) were implanted into the left and right anterior cortex (+1-mm anterior from bregma, 2.5 mm from midline, at the depth of 0.5 mm from the surface of the brain). Permabond gel glue (Permabond Engineering Adhesives Ltd., Hampshire, United Kingdom) was used to fix the electrodes to the skull. Chloridized silver wire reference and ground electrodes were placed subcutaneously in the neck. Heart rate of the animals was preliminary assessed by a pulse oximeter (SA Instruments Inc., Stony Brook, New York). The heartbeat rate of animals was in the range of 360 to 480 beats per minute.

CSD was induced by topical application of 10 μl of 1-M KCl solution (Sigma Aldrich GmbH, Germany) onto occipital cortex area (−6 mm from bregma, 3 mm lateral from midline). The total number of the KCl applications in six animals was 10. In two rats, we applied KCl only in the right hemisphere and in four rats the potassium chloride was applied first in the right hemisphere, then in the left one. One application evoked 1 to 4 CSD waves per experiment. Note that each KCl application was done as a separate statistically independent experiment because it was at least 25-min delay between KCl applications in different hemispheres of the same animal.

All animal procedures were approved by the National Ethical Committee for the Welfare of Laboratory Animals and conducted in accordance with the guidelines set by the European Community Council Directives 86/609/EEC. All means were taken to minimize the number of animals used and their suffering. Rats were group housed with preserved 12-h light/12-h dark cycle and ad libitum access to food and water. After the end of experiment, animals were sacrificed by intravenous injection of saturated K⁺ solution covered with 5% Isoflurane anesthesia.

2.3 Procedure Protocol

Between the end of the surgery and beginning of the measurements all animals were kept in rest during 20 to 30 min to minimize the influence of postsurgical reaction on the obtained results. The duration of one measurement for each animal was 20 min. After initiation of the computer program, the camera began a continuous video recording of the focused area of the cortex. LFP recording was simultaneously started with the camera. After 1 min from the beginning of video recording, a drop (~10 μl) of KCl solution was applied manually using 0.1-ml syringe. Position of the LFP electrodes with respect to the location of KCl application, which is viewed in the video frame of the skull and exposed cortical surface overlaid with the rat's head drawing, is shown in Fig. 1(b).

No manipulation with the animal and setup was done during next 19 min after KCl application while the illuminated cortex was continuously recorded by the camera. Note that both video stream and LFP recording were not interrupted during the KCl application. All the video frames and LFP data were stored in the PC for further processing.

2.4 Blood Pulsation Imaging

The recorded video frames were processed by using custom software implemented in the MATLAB® platform. 2-D mapping of both the blood pulsation amplitude (BPA) and the

relative phase of pulsations (BPP) was calculated using lock-in amplification of every pixel of the recorded video frames synchronously with a cardiac cycle.²⁴ The algorithm consists of two steps: (i) formation of the reference function and (ii) calculation of the correlation matrix representing 2-D distribution of BPA and BPP. The reference function was defined from the recorded frames as follows. We average pixels over the whole area of the open cranial window, which results in the PPG waveform from the whole series of the frames. As known,²⁹ the PPG waveform is temporally modulated at the heartbeat frequency, which allows us to define the duration, T_C , and beginning of each heartbeat. The reference function, $R(t)$, was defined for every cardiac cycle with its specific T_C as

$$R(t) = A_M[\cos(2\pi t/T_C) + i \sin(2\pi t/T_C)]. \quad (1)$$

The coefficient A_M was defined from the condition of the normalization

$$\sum_t \text{Re}[R(t)]\text{Im}[R(t)] = 1, \quad (2)$$

where the summation is conducted over all frames in the cardiac cycle under consideration. Note that it was only the time duration T_C extracted from the PPG waveform, which is needed to define the reference function. The reference function can be also formed from another external signal containing the information about T_C , such as an electrocardiogram (ECG), but the result will be the same. It is well established³⁰ that ECG and PPG define the period of the cardio cycle with high degree of correlation.

Thereafter, we calculated the correlation between temporal variations of each pixel in the series of recorded frames and the above defined reference function, $R(t)$, in the form of a correlation matrix $S_C(x, y)$:

$$S_C(x, y) = \sum_{t=0}^{T_C} I(x, y, t)R(t). \quad (3)$$

Here, $I(x, y, t)$ is a value of the pixel with coordinates (x, y) of the image frame captured at the moment of t . Both $R(t)$ and recorded frames used in Eq. (3) are associated with time moments from the interval of each cardiac cycle with duration T_C . The correlation matrix $S_C(x, y)$ contains the same number of pixels as any of the recorded frames $I(x, y, t)$. The modulus of each pixel value of the $S_C(x, y)$ matrix is proportional to the modulation amplitude of the light reflected back from the respective point at the cortex.²⁴ Since this modulation is caused by the blood pulsations related to the heart activity,³⁰ the modulus of the correlation matrix, $|S_C(x, y)|$, describes the spatial distribution of BPA after normalization with a value from the corresponding location of a time-averaged image matrix. Respectively, the argument of a complex value of the matrix $S_C(x, y)$ describes the spatial 2-D distribution of BPP.

2.5 OISs Imaging

The same recorded frames were also used for calculation of OIS images, which represent 2-D spatial changes of CBV.^{11,16} For visualization of the CSD wave, we calculated the difference image $D(x, y)$ (which is a rate-of-change image) using on the following equation:¹⁶

$$D(x, y) = \frac{I_i(x, y) - I_{i-1}(x, y)}{I_0(x, y)}. \quad (4)$$

Here, $I_0(x, y)$ denotes the initial image just prior to the CSD wave, $I_i(x, y)$ refers to the image at the i 'th time point, and $I_{i-1}(x, y)$ refers to the immediately previous image at the time point $i - 1$. Each $I_i(x, y)$ image was obtained after averaging of the recorded frames within Δt interval to increase the SNR. The time step Δt between adjacent time moments was set to be equal to 40 cardiac cycles of the animal. Therefore, it was dependent on the heartbeat rate and varied in the range of 4 to 6.5 s. The difference imaging was shown to significantly enhance the leading and trailing edges of the CSD wave.¹⁶

3 Results

3.1 Spatio-Temporal Dynamics of Blood Pulsations and OIS Images

From the recorded video frames, we calculated two arrays of the images. First was the series of the correlation matrices $S_C(x, y)$ obtained using Eq. (3), and the second was the series of difference images $D(x, y)$ obtained using Eq. (4). To increase SNR of BPA maps, we averaged the modulus of the correlation matrices (which were calculated for every cardiac cycle of an animal) within Δt equal to 40 cardiac cycles. The same Δt was used for calculating the OIS images. Therefore, the total number of averaged images was the same in both arrays. Any pair of

the images was obtained by different techniques (BPI and OIS imaging) exactly at the same moment of time representing the spatio-temporal dynamics of both blood pulsations and CBV. Typical sequence of BPA maps and OIS images is shown in Fig. 2 in the rows (a) and (b), respectively.

As one can see from the row (b) of Fig. 2, OIS imaging technique reveals the CSD event as a wave originating from the site of topical application of KCl and radially propagating toward the periphery of the cortex. Such a wave was observed and reported by different research groups.^{5,11-14,19} It typically consists of the bright region of increased reflectance due to decrease of CBV, which is followed by the darker hyperperfusion region of decreased reflectance caused by higher absorption of increased CBV. Figure 2(b) shows OIS images recalculated into the change of CBV so that the areas with increased CBV (dilated blood vessels) are colored by the red while those with reduced CBV (constricted vessels) are colored by the blue. For better visualization and analysis we show separately propagation of constriction and dilation waves in rows (c) and (d), respectively.

As seen in Fig. 2(a), an increase of the amplitudes in BPA maps appears after KCl application with the delay of about 90 s, which is approximately the same as for the dilation wave [Fig. 2(d)]. However, simultaneous appearance of BPA and dilative CBV was not observed in all animals. For quantitative estimation of the delay between the different vascular components, we used moments in which these components [being averaged in the regions of interest (ROI) centered with the area of KCl application] reach their extremes. Figure 3 shows the delay between vascular components in different

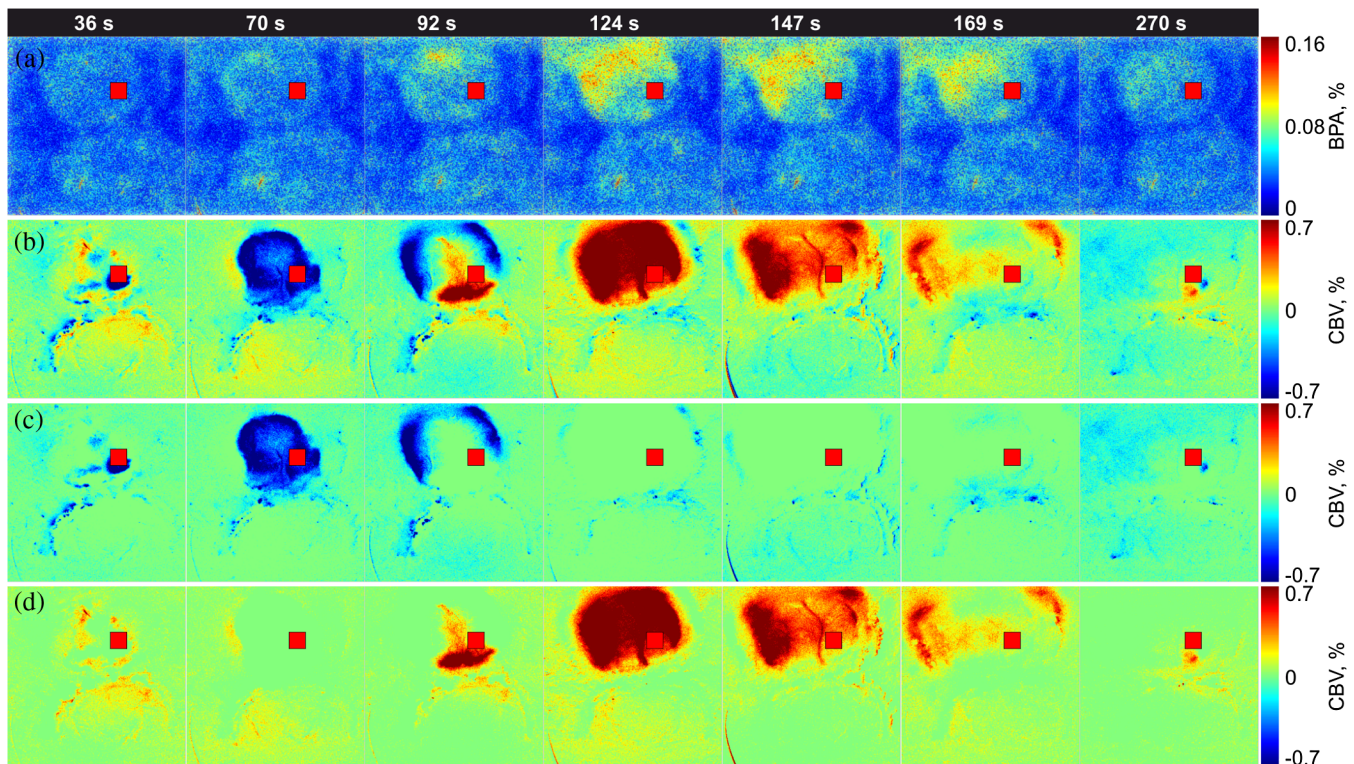


Fig. 2 Comparison of blood pulsations imaging (BPI) and optical intrinsic signal (OIS) images during cortical spreading depression (CSD) wave propagation through the brain cortex of rat #3 from the KCl application site which is marked by the red square: (a) blood pulsation amplitude (BPA) maps; (b) difference OIS images calculated for the same time moments; (c) constrictive; and (d) dilative CBV components of OIS images. Numbers above the columns indicate the time in seconds from the moment of KCl application. The actual size of presented BPA maps and OIS images is $15 \times 15 \text{ mm}^2$.

animals. Symbols in the x -axis encrypt the rat's number and the hemisphere in which KCl was injected: R—the right, and L—the left. Blue squares in Fig. 3(a) are the time when the constrictive wave of the primary CSD event reaches its minimum after KCl application in different rats. As seen, the latent period of the constrictive CBV component varies from 21 to 76 s. However, the delay time between the constrictive and dilative CBV waves is about the same (47 ± 10 s) for all rats as follows from the curve (b), red circles in Fig. 3. In contrast, the delay between the BPA component and dilative CBV component varies not only among different rats but also between different hemispheres of the same rat [see black triangles in Fig. 3(c)]. Note that in rat #1 the BPA wave is in the maximum very late when the dilative CBV wave was completely gone (the delay time is 42 s versus 18.5 s of the half width at the half height of the dilative CBV peak), but sometimes the BPA wave reaches its peak earlier than the dilative wave its dip (negative delay time in Fig. 3).

The BPA maps during their latent period do not differ from the maps calculated during the baseline (before KCl application). Although we did not observe high amplitude in the BPA maps during the baseline, the contours of both cranial windows are distinguishable in the background of all BPA maps compare to near-zero pulsation amplitudes of the skull. This allows us to estimate the SNR of BPA maps during the baseline being in the range of 2 to 3.

It is worth noticing that the increase of BPA does not cover the whole tissue of the cerebral hemisphere, in which the CSD was induced but occurs in the specific limited area in the temporal cortex. Therefore, we concurrently observed two different vascular components of the CSD event: (i) a CBV component visualized by OIS imaging and (ii) a BPA component revealed by BPI. The latter component migrates through the cortical tissue along an unusual trajectory (not radially).

We also evaluated the relative blood pulsation phase maps from the same correlation matrices as the BPA maps by accounting the argument of the matrix values. The variation of the BPP in the relative phase mapping associated with the time interval of the CSD wave was typically 13 ± 3 deg. The variability of the BPP associated with a baseline time interval was at the level of 6 ± 2 deg. This means that the use of the BPP mapping allows observation of the CSD event in parallel with BPA mapping. However, the increase of the BPP values in their maxima during CSD event with respect to variations of BPP during the baseline (before any KCl application) was <2 . This is 5 to 8 times smaller

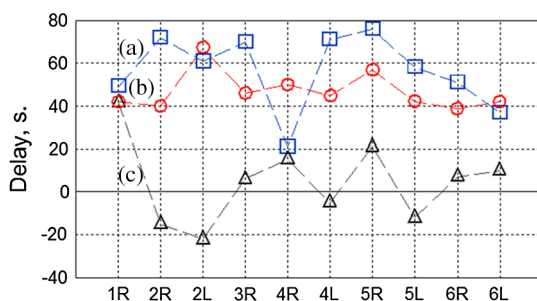


Fig. 3 Delay time of vascular components in different animals: (a) time required for the constrictive CBV component of primary CSD events to reach its dip after KCl application (blue squares); (b) delay time between the peak of the dilative and dip of the constrictive CBV components (red circles); (c) delay time between peaks of BPA and dilative CBV components (black triangles).

than that of the BPA values. Therefore, the following results of the BPI technique are based on the BPA maps only.

3.2 BPA Component of CSD Wave

As shown in Fig. 2(a), the BPA component of the CSD wave propagates mainly through the lateral area of a hemisphere (in the temporal cortex). Moreover, it originates from the place distant from the KCl-application site, which is in contrast with the CBV component originating from the application site. The BPA component is delayed with respect to the CBV component by a delay of about 90 s from the external impact [the image at 92 s in Fig. 2(a)], then it migrates along the cortex towards the animal's nose with the amplitude diminishing after 169 s, and is recovered to the initial amplitude level (during the baseline) after 200 s. In two additional experiments, the CSD was induced in the rostral site close to the animal nose. In these cases, the BPA component propagated again along the similar trajectory in the lateral area of the hemisphere, as during caudal KCl application. However, the CSD propagation was in the opposite direction, toward the animal tail. CBV component in all cases propagated in the form of concentric rings outward the application site.

The trajectory of the BPA component of the CSD wave propagation can be estimated by calculating the coordinates of the “center of mass” of the migrating BPA area in Fig. 2(a). We found that the trajectory line connected the obtained points of the “center of mass” is of bow-shaped form. Such a nonlinear trajectory of the BPA component propagation was observed in all the experiments.

The trajectory of the BPA component can be also visualized by averaging of all correlation matrices during the CSD event [94 to 197 s in Fig. 2(a)]. The temporal averaging of these matrices results in single correlation matrix. The modulus of this matrix describes the spatial distribution of the mean BPA during propagation of the CSD wave. The BPA maps calculated for two different rats are shown in Figs. 4(a) and 4(b). In the same averaged BPA map, we placed the trajectory (black dotted line) obtained by evaluating the coordinates of the “center of mass” as it was described above. These maps show the spatial distribution of the BPA component during its propagation as increased amplitudes zones along the black dotted lines. The direction of the BPA component propagation was outwards the area of the KCl application and toward the anterior cortex of the rat as shown by arrows in Fig. 4. It is worth noting that the BPA component of the CSD wave appears in the same hemisphere, where the KCl was applied: in the right hemisphere in Fig. 4(a) and in the left one in Fig. 4(b).

For comparison, we calculated trajectories of the CBV component by averaging OIS images of the same animals during the CSD event similarly to the BPA trajectories shown in Figs. 4(a) and 4(b). Since CBV component consists of two parts corresponding to constriction and dilation of blood vessels, we averaged these parts separately to exclude their interference. Trajectories of the constrictive and dilative CBV waves are shown in Figs. 4(c) and 4(d) and Figs. 4(e) and 4(f), respectively. As seen, averaging of constrictive (dilative) part of OIS images leads to uniform decreasing (increasing) of the blood volume in a large part of the hemisphere, which confirms the centering spreading of the CBV wave. In contrast, BPA wave propagates in the limited area of the temporal cortex sometimes even in regions, which were not affected by the dilative CBV wave as one can compare Figs. 4(b) and 4(d).

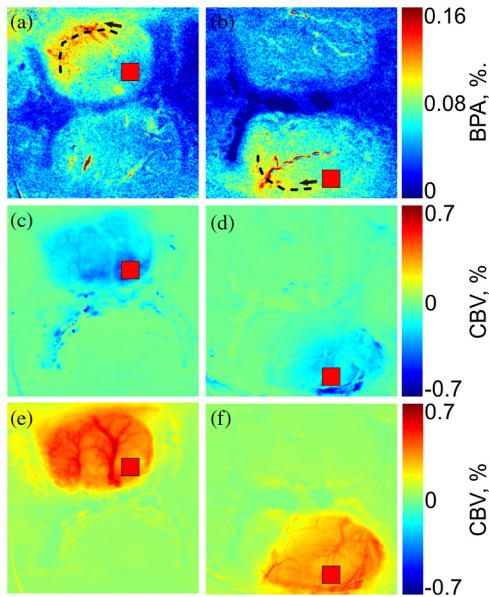


Fig. 4 BPA maps (with the physical size of $15 \times 15 \text{ mm}^2$ at the animal's head) temporally averaged during the whole interval of the CSD wave for rat #3 (a) and rat #4 (b). The wave trajectories are shown by the black dotted line whereas the KCl-application point is shown by the red square. CBV distribution in same rats: (c) and (d) are the constrictive parts of OIS images averaged during the CSD events, and (e) and (f) are similarly averaged dilative parts for rat #3 and rat #4, respectively.

The maximum amplitude within the BPA component of CSD wave trajectory was approximately the same ($0.13 \pm 0.02\%$) in the BPA maps for all rats. Spatial position of the maximal BPA coincides with the area in which the blood vessels of the cortex are visually recognized in the raw frames.

3.3 LFP, OIS, and BPA Time-Traces

In order to collate the CSD wave dynamics revealed by the BPI and OIS methods with LFPs electrophysiological recordings, we represented BPI and OIS results by a time-traces diagram as follows. For BPA maps, we placed a sequence of ROI with the size of 20×20 pixels [Fig. 5(a)] along the evaluated trajectory of the BPA component of the CSD wave. The center of each ROI was placed on the trajectory line of the BPA component [Fig. 5(a)], while the first ROI was centered with the KCl-application point. By calculating the modulus of spatially averaged values within the ROIs in each correlation matrix from the BPA-maps array covered the whole experiment duration (20 min), we obtain time-traces of the BPA component shown in Fig. 5(c). Note that in this calculation, we use correlation matrices obtained in the same way as for BPA maps in Fig. 2.

For OIS images, ROIs of the same size were placed along the radial propagation of the CBV component of the CSD wave [Fig. 5(b)] so that the first and the last ROIs in a sequence were centered with the first and last ones of the BPA maps. By calculating the spatially averaged values within the ROIs in each OIS image, we obtained time-traces of OIS shown in Fig. 5(d). The time range in Figs. 5(c) and 5(d) is diminished to 0 to 400 s aiming to better demonstration of CSD details.

As seen in Fig. 5, BPA experienced 8- to 10-fold increase with respect to the baseline value in the form of a pulse during the CSD event, while the OIS and LFP recordings show a

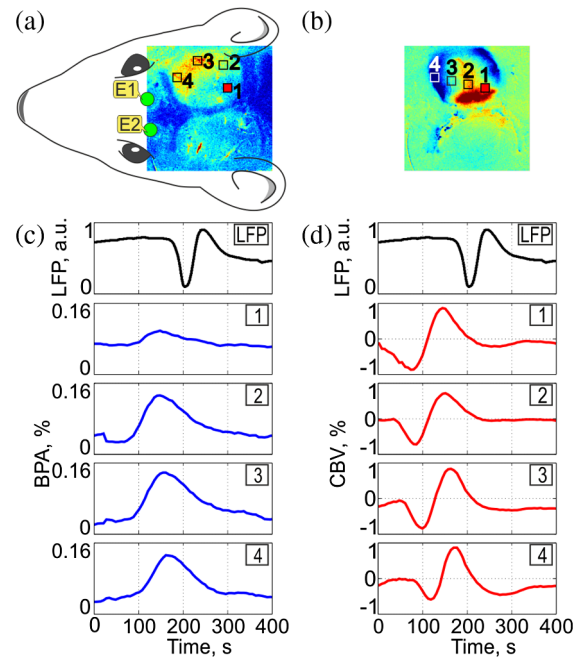


Fig. 5 Schematic view (a) of the animal's head (a) with overlaid averaged BPA map (rat #3) with regions of interest (ROIs) placed along the BPA-wave trajectory. An OIS image (b) of the same rat with ROIs placed along the trajectory of the CBV component. Blue lines, BPA time-traces (c) from ROIs #1-4 shown in the part (a). Red lines, OIS time-traces (d) from ROIs #1-4 shown in the part (b). LFP time-traces (black lines) are shown at the top of (c) and (d). The size of BPA map and OIS image is $15 \times 15 \text{ mm}^2$.

waveform similar to a single period of a sine function (increasing and decreasing for OIS and opposite for LFP in respect to their mean values) during the CSD [Fig. 5(d)]. Note the temporal shift of the BPA and OIS peaks, which indicates the propagation of BPA and CBV waves from one ROI to another in the direction from the KCl application toward the electrode. This leads to the delay in registration of the CSD by LFP in respect to all peaks of BPA maps and OIS images. Considering the trajectories and speed of the vascular components of CSD wave propagation, this delay can be interpreted as additional time needed for the neural component of the CSD wave to cover the distance between the observation area and the LFP-electrode. It is worth noting that the first registration of the BPA component is delayed in respect to the first registration of the constrictive CBV component, while the ending of the CSD event was registered by both BPI and OIS almost simultaneously in rat #3. Therefore, the BPA and constrictive CBV components of the CSD wave propagate through the cortex with different speeds. Considering that the dilative CBV component is delayed with respect to the constrictive one, we also calculated its speed to compare the speed of all vascular components.

3.4 Speed of Vascular Components of the CSD

The propagation speed of all vascular components of the CSD was estimated along the bow-shaped and radial trajectories for BPA and CBV components, respectively. To this end, we plotted the graphs for each observed CSD event so that the time elapsed for traveling from ROI #1 to each ROI in a sequence is shown in the ordinate axis, while the abscissa axis of each graph shows the distance between ROI #1 and each ROI in the sequence. Both sequences consist of 8 ROIs, which allowed us to

check possible speed variations along the trajectories. Note that in Fig. 5, we showed only four representative ROIs from these sequences for simplicity. The first sample in all the graphs (both for BPI and OIS) is logically set to zero. Typical examples of such graphs of the CSD wave dynamics for three components are shown in Fig. 6 for four different animals. Experimental data in Fig. 6 are marked by circles for the BPA component, by squares for the constrictive CBV component, and by triangles for the dilative CBV component. As one can see, these data can be fitted by straight lines which mean that the speeds of all vascular components of the CSD wave are almost constant along their trajectories. The black solid line shows fitting of the experimental data for the BPA component, while the red and blue dashed line show the dilative and constrictive CBV components, respectively. The speed of the observed waves was estimated from the tilt of these straight lines.

In six animals, we excited and observed 10 primary CSD events. The speed of the BPA component varies between 3.00 and 7.29 mm/min. In four rats, the CSD wave was excited in both hemispheres, and each time the speed of the BPA wave was different: in rats #2 and #5 the speed in right hemisphere was bigger than in the left by 13% and 28%, respectively, whereas in rats #4 and #6 it was smaller by 14% and 10%, respectively. We found that there is no big difference between the speeds of constrictive and dilative CBV components. Average relative difference of the speeds for these components calculated for 19 CSD events (including 9 secondary waves) was 3% with the standard deviation of 13%. In 7 cases, the speed of the constriction wave was bigger than that of the dilative wave but in 12 cases it was smaller. The speed of CBV components varied from 1.68 to 4.21 mm/min. For each CSD event, the speed of BPA component was bigger than that of the CBV component. The average relative increase of the BPA-wave speed was 41% with the standard deviation of

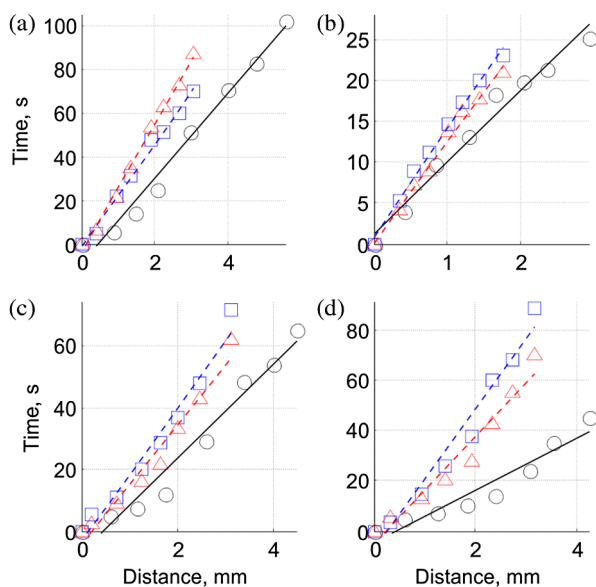


Fig. 6 Diagram of the time elapsed for traveling of vascular components from ROI #1 to each ROI in a corresponding sequence for BPI and OIS techniques for four different animals: (a) rat #1; (b) rat #3; (c) rat #4; and (d) rat #5. Circles, squares, and triangles markers are the experimental data for the BPA, constrictive and dilative CBV components of CSD waves, respectively. Solid and dashed lines indicate the linear fitting of the experimental data.

14%. The minimal increase of the BPA speed (20%) was observed in rat #2, whereas 60% increase was observed in rats #5 and #6.

3.5 Secondary Waves of CSD

Most of the KCl injections (7 of 10) in our experiments evoked more than one CSD wave per one application, which is a commonly described phenomenon.^{13,15,31,32} By performing simultaneously BPI and OIS imaging for the registration of multiple CSD events, we have observed that for every animal, the primary and secondary BPA components of the CSD wave always follow the very same trajectory. As an example, trajectories of the primary and secondary BPA waves in rat #3 and rat #2 are shown in Figs. 7(a) and 7(b) and Figs. 7(c) and 7(d), respectively. These trajectories were calculated by averaging BPA maps during the respective CSD event. As one can see in Fig. 7, the morphology of the images is the same within each of pairs (a, b) and (c, d). However, there is visible difference in the amplitude of the maps: BPA of the primary event is a bit bigger than secondary. We also noticed that the secondary CBV component starts from the point which does not coincide with the initial KCl-application site from which the primary CBV wave typically originates.

In order to compare the results of the CSD wave detection by LFP, BPI, and OIS techniques, we plotted in Fig. 8 time-traces of the BPA and CBV values spatially averaged within the ROI #1 (20 × 20 pixels) centered with the place of KCl application together with the LFP traces. Due to the specific of animals' preparation, the LFP electrodes were fixed to the skull outside the cranial window. Consequently, an additional time was needed for the neuronal component (measured by LFP) to cover the distance between the ROI #1 and the recording electrode. Assuming that the speed of the CBV component is about the same as the speed of the neuronal component measured by LFP,^{13,15,19} we can reconstruct the initial moment of the LFP-dip appearance at the place of the ROI #1. Such a reconstruction shows that the neuronal component always precedes both all vascular CSD components: the delay between the reconstructed LFP and constrictive CBV component (which always appears the first among vascular components, see Sec. 3.4) is in the range of 12 to 69 s.

As seen in Fig. 8, the BPA component is always delayed with respect to the constrictive CBV component for both primary and

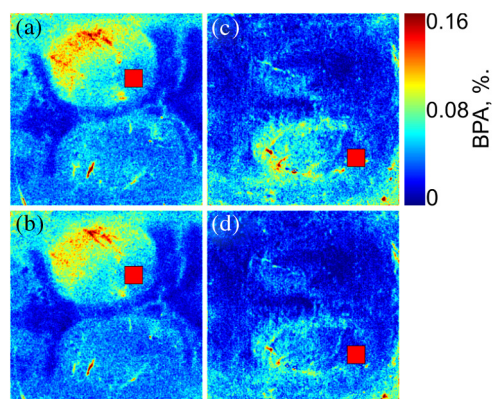


Fig. 7 BPA maps averaged during the whole interval of the primary (a, c) and secondary (b, d) CSD waves in two animals (rat #2 in the left and rat #3 in the right).

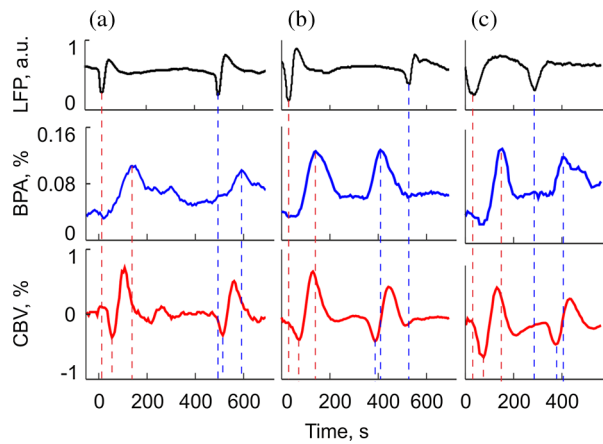


Fig. 8 Time traces with primary and secondary CSD observed in BPI (blue lines), OIS (red lines), and LFP (black lines) for rat #1 (a) rat #3 (b), and rat #5 (c). BPI and OIS time-traces were evaluated in the ROI #1 centered with the KCl application. The time scale of the LFP signal was recalculated to the position of ROI #1. Relative position in the time scale of signals extremes is indicated by the red and blue dashed lines for primary and secondary CSD events, respectively.

secondary CSD waves. This delay varies for different animals in the range between 16 and 97 s. It may either increase from 46 s for the primary CSD event to 80 s for the secondary event in the rat #6 or decrease from 78 to 28 s in rat #5, or show small changes (from 84 to 97 s) in rat #1. Note that during the secondary CSD event in rat #3 [Fig. 8(b)], all vascular components appear 260 s earlier than the LFP signal. The situation is opposite for the secondary event in rat #5 where the constrictive CBV component is delayed with respect to the LFP dib by 160 s, while in rat #1, the LFP and constrictive CBV waves appear simultaneously.

4 Discussion

In this study, we describe for the first time the novel vascular component of CSD in the brain cortex. This was essentially possible because we combined in the same experiment two modes of live imaging, namely recently developed BPI and traditional OIS. BPI and OIS imaging systems are based on the same experimental data (the same series of the recorded frames) but differ only in the data processing, which leads to visualization of different aspects of the vascular dynamics. Although OIS reveals changes of the CBV,^{4,5} BPI reveals the pulsations amplitude of blood vessels at the heartbeat frequency.²⁴ The results of our study show that even though both the BPA and CBV components characterize the same vascular system, they are not directly related with each other. This statement is supported by the observation during the CSD events of completely different trajectories for CBV and BPA components of the CSD wave (concentrically expanded rings and bow-shaped curve, respectively), different propagation speed of these components (see Fig. 6), and different time delay between them (see Fig. 3). Perhaps, the vascular architecture and layout relative to location of the craniotomy may determine the BPA trajectory observed. However, an additional research is required to verify this suggestion. In this article, we just report observation of previously hidden vascular component.

At the moment, we cannot specify the neurovascular mechanism responsible for pulsations of the blood vessels at the heartbeat frequency. This topic certainly requires more detailed

studies with concurrent use of the wide range of imaging techniques including BPI. Our research has just provided first experimental evidence of the fact that pulsations of the blood vessels are controlled by the neural system in a different way than the relatively slower dilatation or constriction of the same vessels.

As we recently reported, serious asynchronicity (up to 150 deg of the phase difference between blood pulsations in the left and right sides of the face) of facial blood perfusion was revealed by the BPI technique in migraineurs during the interictal period.³³ Therefore, we paid special attention to analysis of BPP maps in our experiments. Nevertheless, no significant phase difference was observed between the left and right hemispheres of the rat's cortex either before or after CSD event. However, CSD wave can be also visualized in the BPP maps, which means appearance of the average phase difference of 13 deg (which is two-folds larger than the occasional phase variations) between the area with higher BPA and the rest of the cortex. It should be underlined that in all our experiments no BPA/BPP changes have been observed in the nonexcited hemisphere of the cortex in-line with LFP registrations. On the one hand, absence of asynchronicity between the hemispheres is explained by the fact that the tested animals did not suffer from migraine in contrast with migraineurs studied in Ref. 33. On the other hand, appearance of asynchronicity during CSD event may be caused by a relationship between CSD and migraine and likely depends on abnormal autonomous control of the vascular bed.³³

In conclusion, we have demonstrated that the CSD phenomenon is accompanied by the wave of increasing amplitude of pulsations of blood vessels, which covers a limited area of the cortex and always propagates with the stereotypic bow-shaped trajectory. This type of wave propagation is in strong contrast with commonly observed wave of vascular changes, which concentrically spreads out from the point of excitation in all directions and covers the whole cortex. Moreover, the blood-pulsating wave starts with the delay of 20 to 90 s after the constrictive vascular wave, and it propagates through the cortex with the higher speed (by 40%). The observed discrepancy of BPI and OIS images indicates the important role of the blood-pulsating component in the CSD event (measured by BPI technique), invisible with other imaging techniques. The fact that the BPI technique relies on the BPA, which is not measured by commonly used imaging methods, allows obtaining the results which provide novel information concerning dynamic processes underlying several major neurological diseases as migraine, stroke, and brain trauma. Considering the prior importance of the study and diagnostics of these diseases, BPI can serve as a valuable tool for preclinical neurobiological and pathophysiological research.

Acknowledgments

This work is supported by the Academy of Finland (projects no. 136881 and 135179). Ph.D. Igor Sidorov from the Department of Applied Physics, University of Eastern Finland is acknowledged for useful discussion.

References

1. A. Gorji, "Spreading depression: a review of the clinical relevance," *Brain Res. Rev.* **38**(1-2), 33-60 (2001).
2. A. Leão, "Spreading depression of activity in cerebral cortex," *J. Neurophysiol.* **7**(6), 359-390 (1944).

3. L. Marshall et al., "Changes in direct current (DC) potentials and infra-slow EEG oscillations at the onset of the luteinizing hormone (LH) pulse," *Eur. J. Neurosci.* **12**(11), 3935–3943 (2000).
4. R. D. Frostig et al., "Cortical functional architecture and local coupling between neuronal activity and the microcirculation revealed by in vivo high-resolution optical imaging of intrinsic signals," *Proc. Natl. Acad. Sci. U. S. A.* **87**(16), 6082–6086 (1990).
5. Y. Tomita et al., "Repetitive concentric wave-ring spread of oligemia/hyperemia in the sensorimotor cortex accompanying K⁺-induced spreading depression in rats and cats," *Neurosci. Lett.* **322**(3), 157–160 (2002).
6. A. Shatillo et al., "Cortical spreading depression induces oxidative stress in the trigeminal nociceptive system," *Neuroscience* **253**, 341–349 (2013).
7. G. G. Somjen, "Mechanisms of spreading depression and hypoxic spreading depression-like depolarization," *Physiol. Rev.* **81**(3), 1065–1096 (2001).
8. A. Leão, "Pial circulation and spreading depression of activity in the cerebral cortex," *J. Neurophysiol.* **7**(6), 391–396 (1944).
9. M. Unekawa et al., "Sustained decrease and remarkable increase in red blood cell velocity in intraparenchymal capillaries associated with potassium-induced cortical spreading depression," *Microcirculation* **19**(2), 166–174 (2012).
10. K. C. Brennan et al., "Distinct vascular conduction with cortical spreading depression," *J. Neurophysiol.* **97**(6), 4143–4151 (2007).
11. A. M. O'Farrell et al., "Characterization of optical intrinsic signals and blood volume during cortical spreading depression," *Neuroreport* **11**(10), 2121–2125 (2000).
12. A. M. Ba et al., "Multiwavelength optical intrinsic signal imaging of cortical spreading depression," *J. Neurophysiol.* **88**(5), 2726–2735 (2002).
13. M. Tomita et al., "Initial oligemia with capillary flow stop followed by hyperemia during K⁺-induced cortical spreading depression in rats," *J. Cereb. Blood Flow Metab.* **25**(6), 742–747 (2005).
14. M. Guiou et al., "Cortical spreading depression produces long-term disruption of activity-related changes in cerebral blood volume and neurovascular coupling," *J. Biomed. Opt.* **10**(1), 011004 (2005).
15. S. Chen et al., "Time-varying spreading depression waves in rat cortex revealed by optical intrinsic signal imaging," *Neurosci. Lett.* **396**(2), 132–136 (2006).
16. S. Chen et al., "In vivo optical reflectance imaging of spreading depression waves in rat brain with and without focal cerebral ischemia," *J. Biomed. Opt.* **11**(3), 034002 (2006).
17. C. Yin et al., "Simultaneous detection of hemodynamics, mitochondrial metabolism and light scattering changes during cortical spreading depression in rats based on multi-spectral optical imaging," *Neuroimage* **76**, 70–80 (2013).
18. A. K. Dunn et al., "Dynamic imaging of cerebral blood flow using laser speckle," *J. Cereb. Blood Flow Metab.* **21**(3), 195–201 (2001).
19. C. Ayata et al., "Pronounced hypoperfusion during spreading depression in mouse cortex," *J. Cereb. Blood Flow Metab.* **24**(10), 1172–1182 (2004).
20. A. K. Dunn, "Laser speckle contrast imaging of cerebral blood flow," *Ann. Biomed. Eng.* **40**(2), 367–377 (2012).
21. J. Sonn and A. Mayevsky, "Effects of brain oxygenation on metabolic, hemodynamic, ionic and electrical responses to spreading depression in the rat," *Brain Res.* **882**(1–2), 212–216 (2000).
22. F. P. Wieringa, F. Mastik, and A. F. W. van der Steen, "Contactless multiple wavelength photoplethysmographic imaging: a first step toward "SpO₂ camera" technology," *Ann. Biomed. Eng.* **33**(8), 1034–1041 (2005).
23. K. Humphreys, T. Ward, and C. Markham, "Noncontact simultaneous dual wavelength photoplethysmography: a further step toward noncontact pulse oximetry," *Rev. Sci. Instrum.* **78**(4), 044304 (2007).
24. A. A. Kamshilin et al., "Photoplethysmographic imaging of high spatial resolution," *Biomed. Opt. Express* **2**(4), 996–1006 (2011).
25. A. A. Kamshilin et al., "Variability of microcirculation detected by blood pulsation imaging," *PLOS One* **8**(2), e57117 (2013).
26. H. Ma, M. Zhao, and T. H. Schwartz, "Dynamic neurovascular coupling and uncoupling during ictal onset, propagation, and termination revealed by simultaneous in vivo optical imaging of neural activity and local blood volume," *Cereb. Cortex* **23**(4), 885–899 (2013).
27. R. S. Stewart et al., "Spontaneous oscillations in intrinsic signals reveal the structure of cerebral vasculature," *J. Neurophysiol.* **109**(12), 3094–3104 (2013).
28. W. Cui, L. E. Ostrander, and B. Y. Lee, "In vivo reflectance of blood and tissue as a function of light wavelength," *IEEE Trans. Biomed. Eng.* **37**(6), 632–639 (1990).
29. J. Allen, "Photoplethysmography and its application in clinical physiological measurement," *Physiol. Meas.* **28**(3), R1–R40 (2007).
30. N. Selvaraj et al., "Assessment of heart rate variability derived from finger-tip photoplethysmography as compared to electrocardiography," *J. Med. Eng. Tech.* **32**(6), 479–484 (2008).
31. V. B. Bogdanov et al., "Migraine preventive drugs differentially affect cortical spreading depression in rat," *Neurobiol. Dis.* **41**(2), 430–435 (2011).
32. V. B. Bogdanov et al., "Behavior in the open field predicts the number of KCl-induced cortical spreading depressions in rats," *Behav. Brain Res.* **236**(1), 90–93 (2013).
33. N. Zaproudina et al., "Asynchronicity of facial blood perfusion in migraine," *PLOS One* **8**(12), e80189 (2013).

Victor Teplov is a PhD student in the Department of Applied Physics, University of Eastern Finland, Kuopio, Finland. He graduated from Moscow National Research Nuclear University "MEPhI" (Russia) in 2004 with an MSc degree. Since 2008, he has been doing research in the field of multispectral imaging. His research interest includes blood pulsation imaging, optical sensors, and multispectral imaging.

Artem Shatillo graduated from Kharkov National Medical University of Ukraine in 2005. He obtained specialization in clinical psychiatry in 2007. Since 2009, he has been a postgraduate student in the Biological Nuclear Magnetic Resonance research group in the Department of Neurobiology, A. I. Virtanen Institute for Molecular Medicine, University of Eastern Finland, Kuopio, Finland. His research areas are cortical spreading depression, migraines, and functional MRI.

Ervin Nippolainen graduated in 1997 with a degree in physics and received his PhD in 2000 from the University of Joensuu, Finland. In 2004, he joined the Department of Applied Physics, University of Eastern Finland, where he is currently employed as a researcher. His research interests include optical sensors, blood pulsation imaging systems, photoplethysmography, and electro-optical materials.

Olli Gröhn is a professor of biomedical NMR and director of the Biomedical Imaging Unit at the A. I. Virtanen Institute for Molecular Sciences at the University of Eastern Finland. He has 20 years of experience in development of magnetic resonance imaging and other imaging techniques for assessment of different neurological disease models, which is still his major research interest area.

Rashid Giniatullin is a professor of cell biology in the AIV Institute for Molecular Medicine at the University of Eastern Finland. He obtained his PhD in physiology at the Kazan Medical University in 1981 and still collaborates with Kazan scientists. His current focus is on pathophysiology of migraine and, in particular, on mechanisms of cortical spreading depression (CSD) associated with migraine aura.

Alexei A. Kamshilin received his MSc from Leningrad State University in 1974 and a PhD from A.F. Ioffe Institute (Leningrad, USSR) in 1982. His academic career started in 1974 in Russia, continued in Brazil in 1990 to 1992, and since 1992 he has been researching in Finland. Since 2004, he has been a professor at the University of Eastern Finland (Kuopio). His research interest includes nonlinear and coherent optics, optical sensors technology, and multispectral imaging for biomedical applications.